Supporting Information for

Processing-structure-performance relationships of microporous metal-organic polymers for size-selective separations

Jen-Yu Huang[1], Yuanze Xu[1], Phillip J. Milner[2], Tobias Hanrath[1]*

[1]Robert F. Smith School of Chemical and Biomolecular Engineering, Cornell University, Ithaca, NY 14853, USA
[2] Department of Chemistry and Chemical Biology, Cornell University, Ithaca, NY 14853, USA

* E-mail: tobias.hanrath@cornell.edu

Table of Content

1. ADDITIONAL CHARACTERIZATION OF BUILDING BLOCKS

$[Zr_6O_4(OH)_4](MAA)_{12}$ (Zr-MAA) was synthesized and dispersed in toluene as colloidal nanoclusters. The building unit was characterized by Powder X-ray diffraction (PXRD), Fourier transform infrared spectroscopy (FTIR) and Nuclear magnetic resonance (NMR). First, the PXRD pattern in Figure S1a demonstrates that synthesized material remains crystalline and possesses peaks at 5.9° and 7.6°, similar to previous reports[1]. Second, the compositions of Zr-MAA closely match the composition of zirconium methacrylate obtained by Fourier transform infrared spectroscopy (FTIR) in Figure S1b. The Zr-O vibration could be observed around 600 cm^{-1}. The symmetric and asymmetric COO^- vibrations represent coordinated methacrylates to the Zr-oxide core. Last, Figure S1c shows the ^1H NMR spectra for Zr-MAA. The signals at 6.14 and 5.55 ppm correspond to the two hydrogens on methacrylate. Signals at 3.65 and 4.1 are related to the Zr-OH. Signals around 1.86 and 0.95 are CH_3 in methacrylate. In addition, we couldn't observe the OH signal around 12 ppm, supporting the binding of the ligands. The discussed analyses back the conclusion of successfully synthesized Zr-MAA building blocks. Solubility and other information can be found in our previously reported work[2].

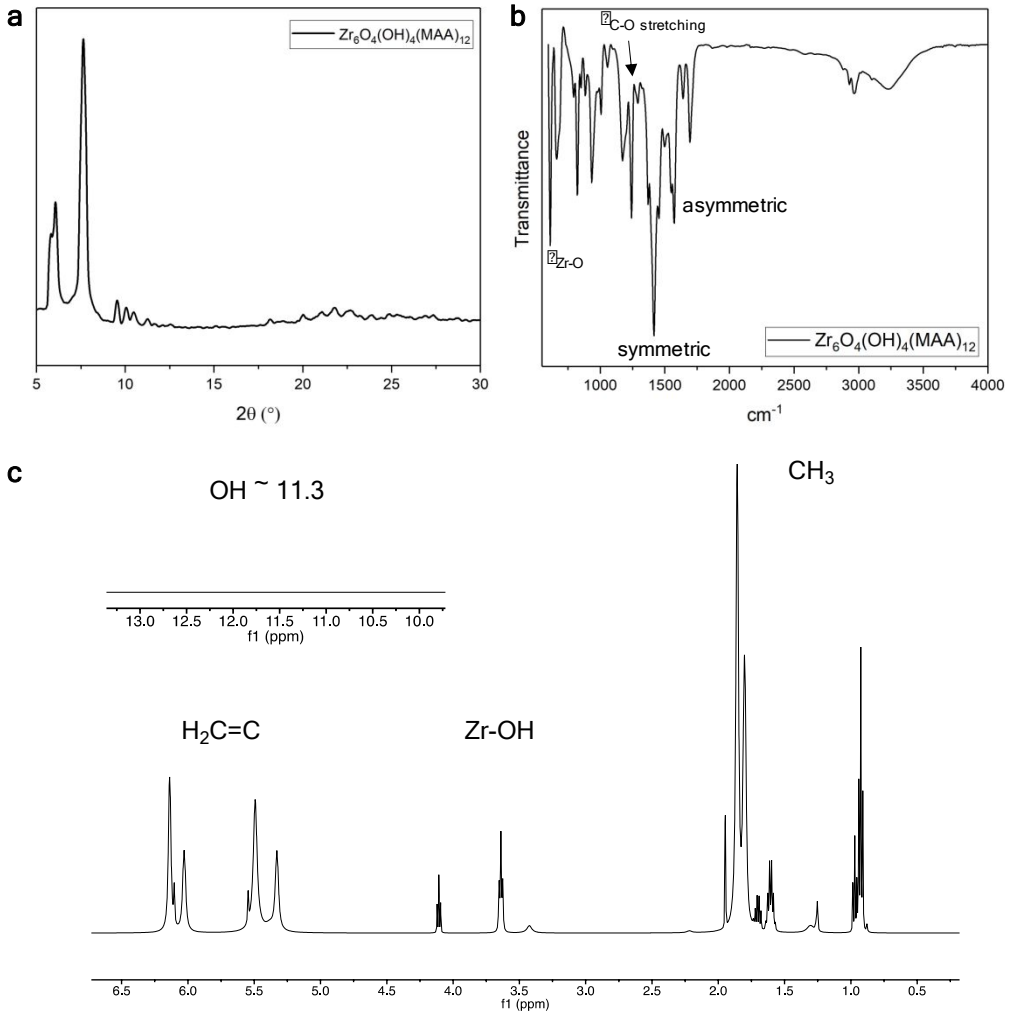

Figure S1. Characterization of Zr-MAA building units by **a,** PXRD, **b,** FTIR and **c,**^1H NMR (500 MHz, Chloroform-*d*).

2. PHOTO-INITIATED POLYMERIZATION PROCESS

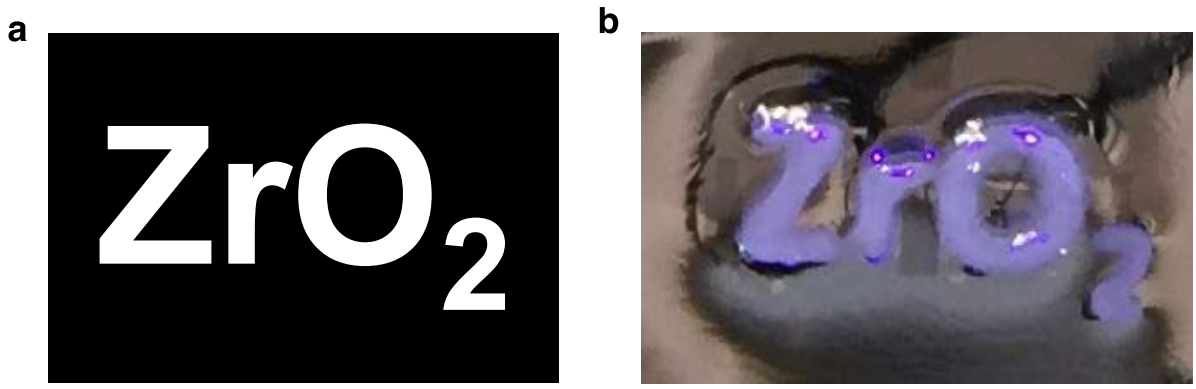

Figure S2. Example of **a,** a projection pattern and **b,** photograph of the resulting printed part with near UV light from a commercial projector.

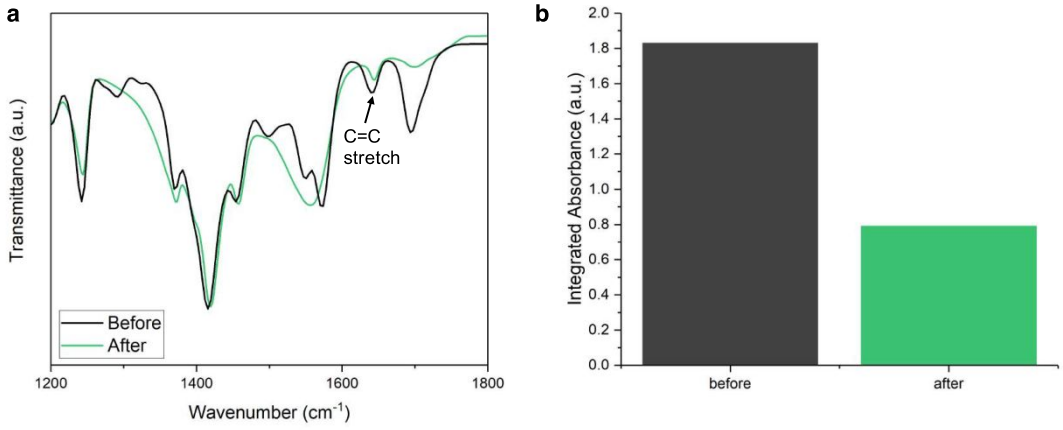

Figure S3. **a,** FTIR transmission spectra of the Zr-MAA before and after photopolymerization. The stretching vibration of the C=C double bond at 1630 cm^{-1}. The C=C band was then integrated (from 1620 cm^{-1} to 1650 cm^{-1}) and the values are reported in **b** exhibiting a decrease as expected from polymerization.

3. ASSEMBLY OF BUILDING UNITS

Because the building blocks are similar to UiO-66, we originally hypothesized they may assemble in the same way into tetrahedral, cubic, octahedral, or other topologies. We expect to see randomly formed polyhedra shown in Figure S4b and c. However, we only observed signals at around 6Å, which suggests the building blocks intend to assemble in a specific way. We think the phenomenon arises due to the irreversible reaction, which doesn't provide freedom for molecules to assemble and reassemble. The irreversible reactions also explain the formation of small grain sizes and secondary mesopores as shown in Figure S5. Stacking of grains and spacing between these grains can be seen in Figure S5a and b, respectively. In addition, empty regions are tertiary mesopores formed by phase separation.

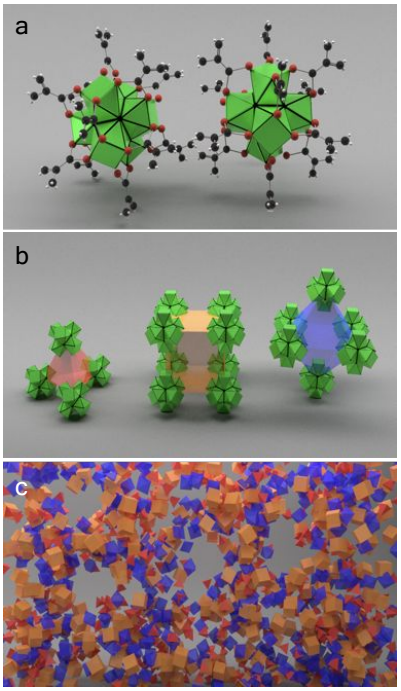

Figure S4. a, Models of two Zr-MAA clusters. **b,** Possible arrangement of building blocks into tetrahedral, cubic, or octahedral units and **c,** Random formation of polyhedral subunits.

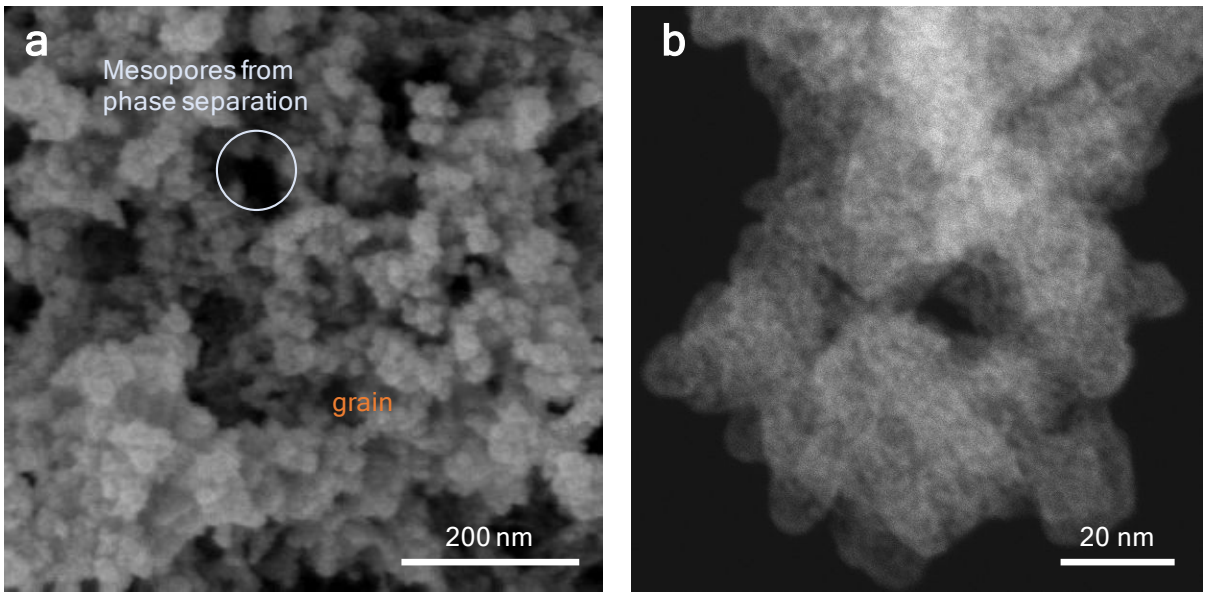

Figure S5. a, SEM image showing grains and tertiary mesopores made from phase separation. **b,** TEM image showing grains in detail and spacing between them.

4. BET CONSISTENCY AND KINETICS OF GAS SORPTION

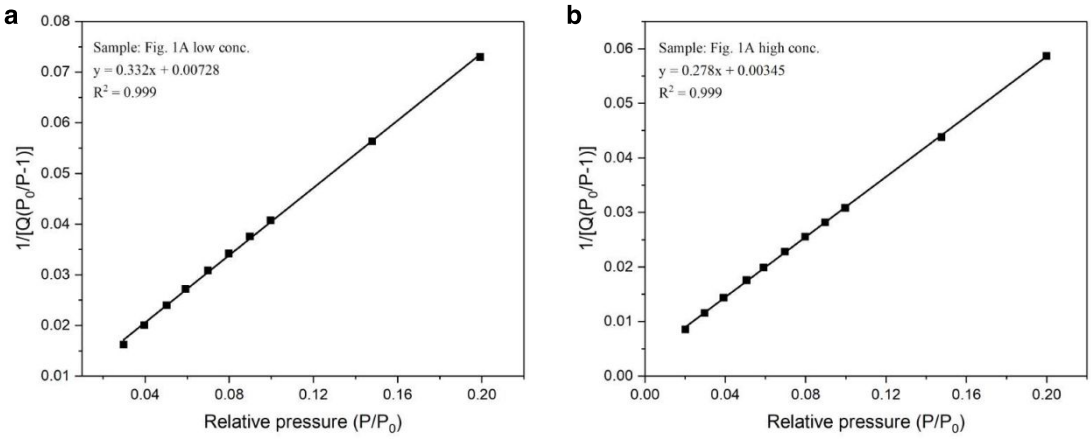

Figure S6. BET consistency of samples prepared with different ink concentration.

To probe the effect of pore size distribution on adsorption kinetics, we carried out some rate of adsorption experiments. We used the same two samples in Figure 1, which are prepared with high and low concentration of Zr-MAA. We dosed toluene into the samples and observed whether hierarchical porosities affect the kinetics of adsorption. However, the result in Figure S7 seems quite similar, suggesting hierarchical porosities do not play much of a role in the case of gas species. We infer that mesopores are relatively big compared with gas species, so their relative sizes do not affect the kinetics of adsorption.

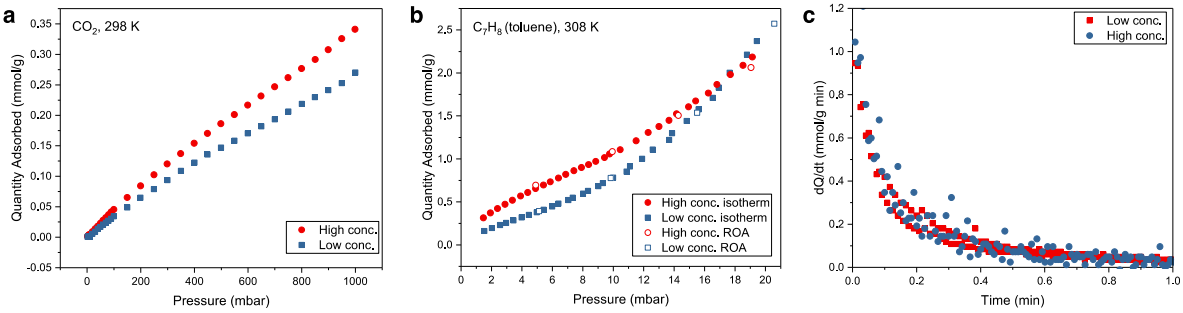

Figure S7. a, CO_2 sorption isotherms at 298K and **b,** toluene sorption isotherms at 308K of samples in Figure 1a. **c,** Rates of toluene adsorption on superstructures with different pore size distributions.

5. DEVICE FABRICATION

This section aims to provide more details about device fabrication. In general, the workflow is to set up moldings, add Zr-MAA solution, expose the solution to UV light, and then wash the solid material. Figure S8 and S9 show fabricated devices and setup. The mechanical strength of the material can be referenced to our previous work[2]. In addition, the mechanical strength can be potentially tuned for the desired properties by mixing with other oligomers normally found in a 3D printing ink. After washing and confirming the cleanliness with UV-vis, devices can be connected with a syringe pump for separation. Figure S10 shows the chemical structure of targeted compounds. Figure S11b shows the differences in UV-vis before and after washing. In addition, UV-vis can provide some information of drug and NDMA concentration (220-240 nm) as shown in Figure S11a. However, because the signals of the drug and NDMA overlap, we don't recommend using Uv-vis for quantitative purposes.

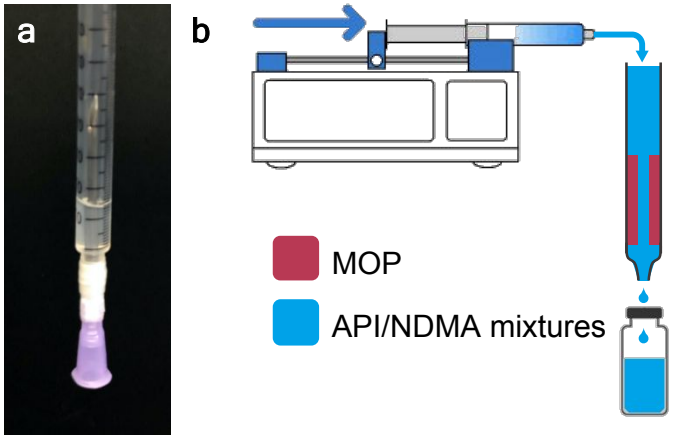

Figure S8. a, A device prepared with molding method. **b,** Schematic explanation of the setup.

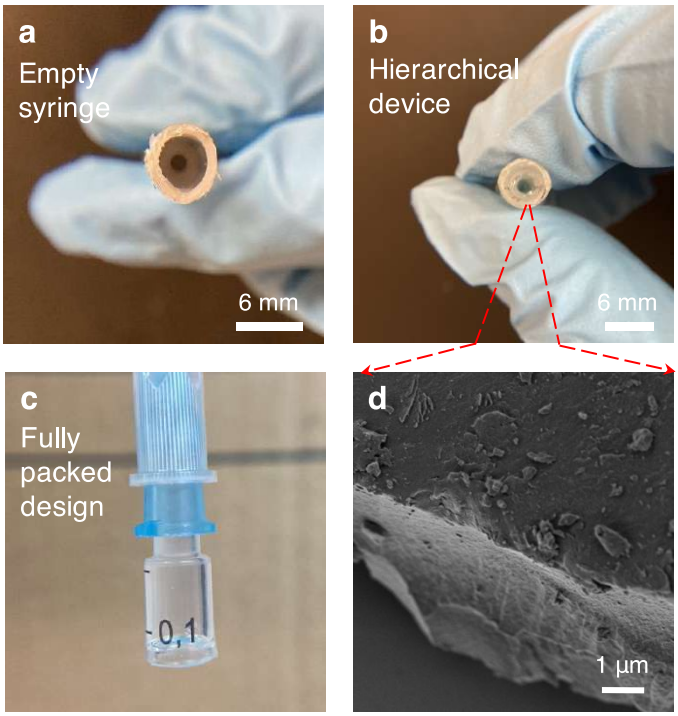

Figure S9. Images of **a,** an empty syringe, **b,** a hierarchical device (inner diameter: 2 mm; outer diameter: 4 mm), and **c,** a fully-packed column. **d,** SEM image of the dried pieces.

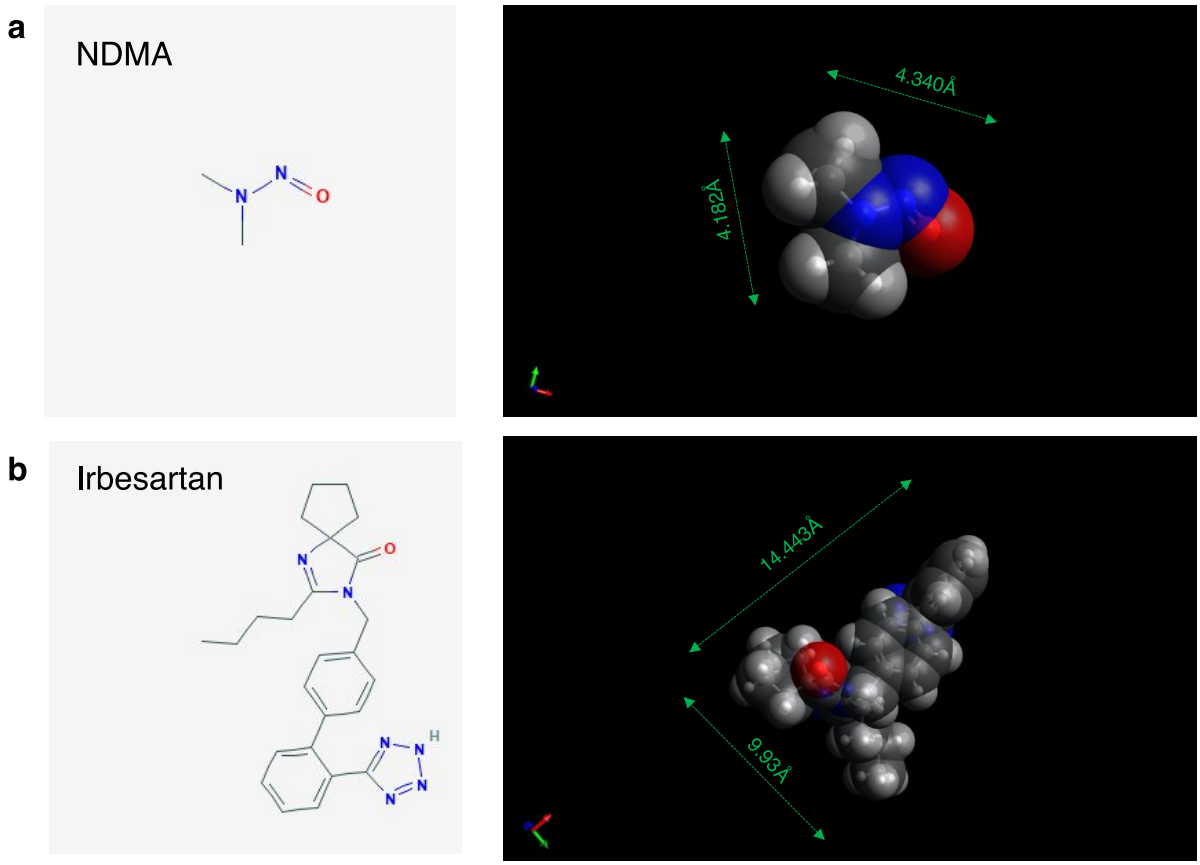

Figure S10. Molecular structure and computed 3D models of **a,** NDMA and **b,** Irbesartan.

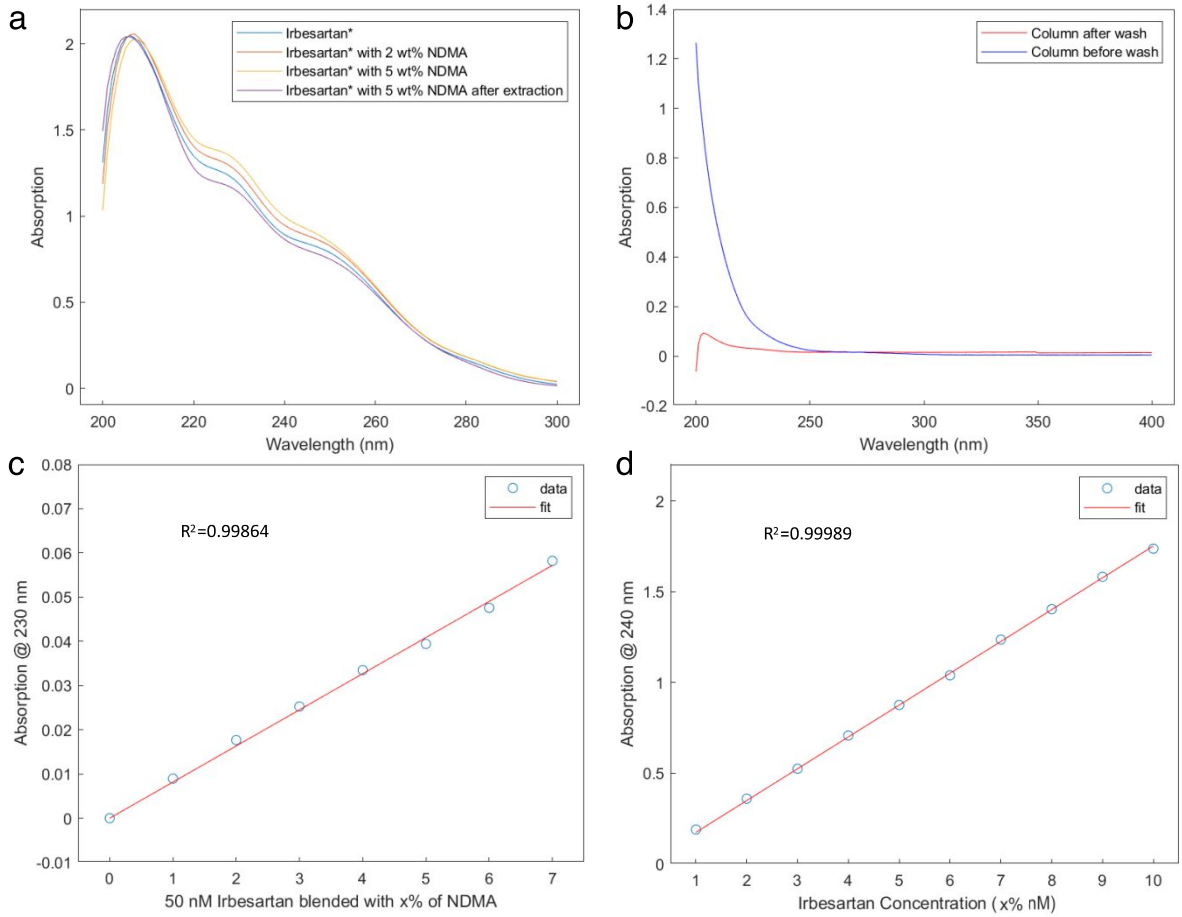

Figure S11. Uv-vis data of **a,** different concentrations of NDMA before and after separation. **b,** devices before and after wash. **c,** and **d,** shows the linear consistency of Irbesartan and NDMA's concentration.

6. ADDITIONAL SEPARATION STUDIES

This section aims to provide more details regarding approaches to monitor concentration and additional information in our optimization process.

NMR is a good method for preliminary studies because of the convenience to monitor Irbesartan and NDMA at the same time. Therefore, we used NMR in our initial studies to confirm the hypothesized NDMA adsorption in fully-packed columns. Figure S12 shows signals of Irbesartan, NDMA, and separation performances. In terms of the operation of full pack columns, we found it was time-consuming to wash these columns because of high back pressure. We usually had to wash overnight to make sure the cleanliness. Besides, there were cracks showing up in full pack columns sometimes during cleaning procedures because of solvent evaporation. Although taking care of full pack columns is a bit tedious, we validated our hypothesis to use micropores to separate contaminates. Overall speaking, NMR is a quick way to check existence of drug and NDMA, but GC may be better to quantify concentration of NDMA.

We followed reported GC methods to better quantify concentration of NDMA. First, we did two sets of control experiments ranging from 1 to 1000 ppm to calibrate GC. Figure S13a shows integral area of different NDMA concentrations. We directly extracted integral results from chromatograms (peak @ ~2.3min) without any internal standard. Further, we used a suggested method with dodecane (peak @ ~6.8min) as the internal standard. We added the same amount

of dodecane in all samples. Figure S13b shows the normalized integral area of NDMA to dodecane. Both methods show great consistency. All NDMA separation studies in hierarchically designed devices were done and analyzed with internal standard approach.

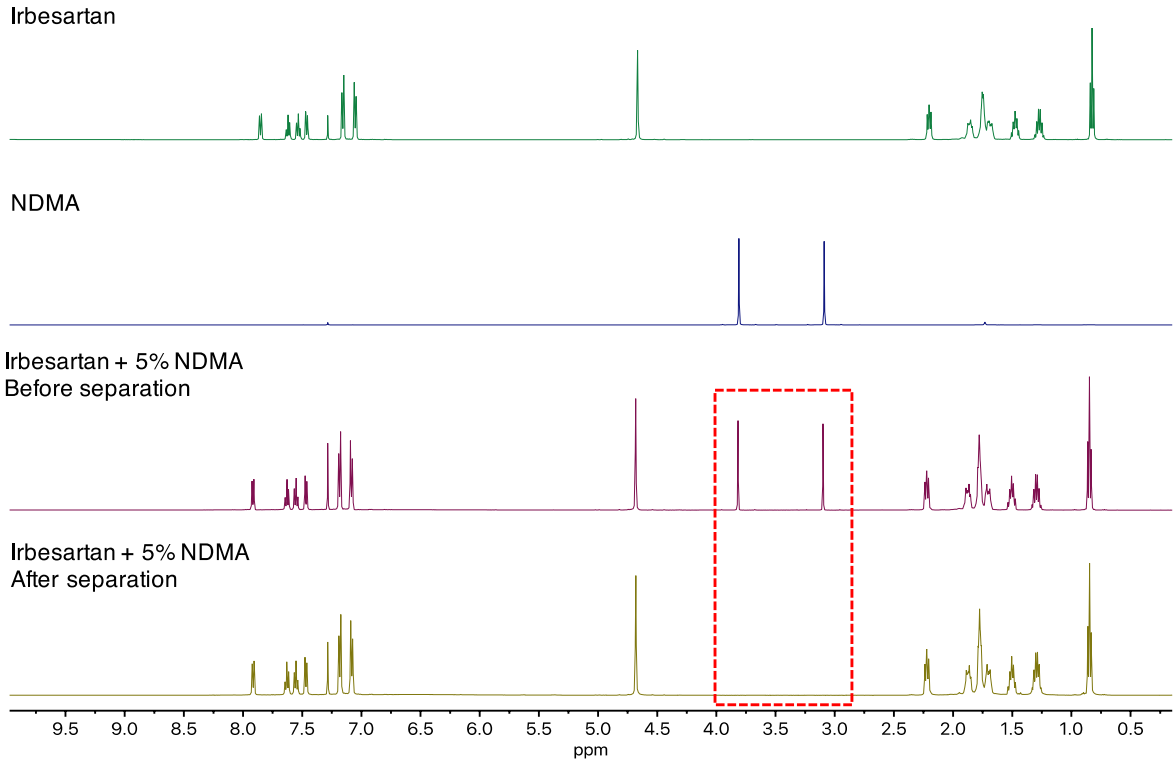

Figure S12. NMR of Irbesartan and NDMA before and after separation (full pack column).

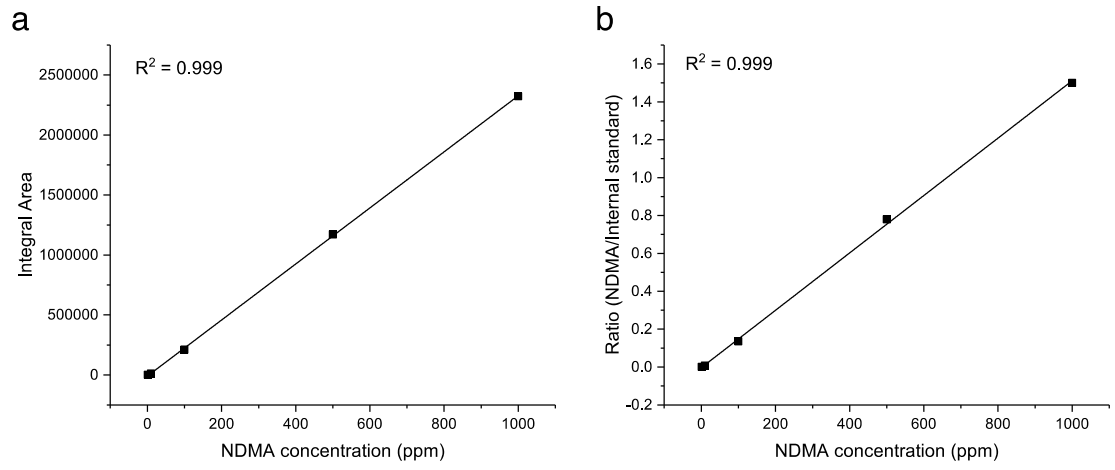

Figure S13. Consistency of NDMA concentration measurements **a,** without and **b,** with internal standard.

7. ANALYTICAL MODEL

A simplified analytical modal was calculated to help the evaluation of significant factors for device's optimization. The analytical model is calculated based on Navier-Stokes equations, Darcy's law and mass balance by following Granger's method[3]. Basically, we first introduced governing equations, then rewrote the equations in dimensionless forms and brought in the boundary conditions. The model is schematically shown in Figure S14. The calculation is done on the following assumptions:

- Lamina flow, steady state, incompressible
- Fully developed velocity profile
- No slip condition at the porous wall

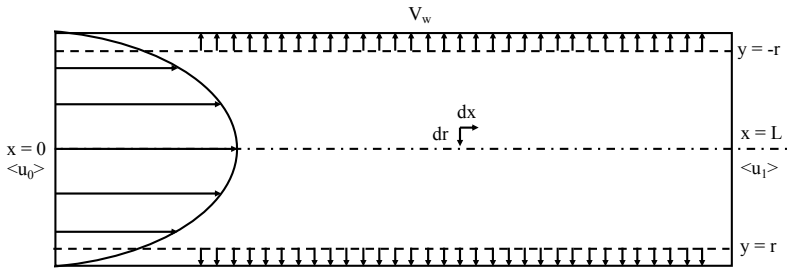

Figure S14. Schematic diagram of laminar flow in a tubular channel with porous wall.

Governing equations are described as following:

$$\frac{1}{r}\frac{\partial}{\partial r}(ru_r) + \frac{\partial}{\partial x}(u_x) = 0 \quad (1)$$

$$\rho\left\{u_r\frac{\partial u_x}{\partial r} + u_x\frac{\partial u_x}{\partial x}\right\} = -\frac{\partial p}{\partial x} + \mu\left\{\frac{1}{r}\frac{\partial}{\partial r}\left(r\frac{\partial u_x}{\partial r}\right) + \frac{\partial^2 u_x}{\partial x^2}\right\} \quad (2)$$

$$\rho\left\{u_r\frac{\partial u_r}{\partial r} + u_x\frac{\partial u_r}{\partial x}\right\} = -\frac{\partial p}{\partial r} + \mu\left\{\frac{\partial}{\partial r}\left(\frac{1}{r}\frac{\partial}{\partial r}(ru_r)\right) + \frac{\partial^2 u_r}{\partial x^2}\right\} \quad (3)$$

$$\pi R^2\langle u_x\rangle = \pi R^2\left(\langle u_x\rangle + \frac{\partial u_x}{\partial x}dx\right) + \frac{\kappa}{\mu}(\langle p\rangle - p_0)2\pi R dx \quad (4)$$

Dimensionless form:

$$X = \frac{x}{R} \quad (5)$$

$$Y = \frac{r}{R} \quad (6)$$

$$\langle P\rangle = \frac{\langle p\rangle - p_0}{p_0} \quad (7)$$

$$\langle U_x\rangle = \frac{\langle u_x\rangle}{\langle u_0\rangle} \quad (8)$$

$$Re = \frac{2\rho\langle u_0\rangle R}{\mu} \quad (9)$$

$$F = \frac{p_0 e}{12\mu\langle u_0\rangle}\langle P\rangle \quad (10)$$

Boundary conditions:

$$U_Y(X,0) = 0 \quad (11)$$

$$U_X(X,1) = 0 \quad (12)$$

$$U_Y(X,1) = M^2F(X,1) \quad (13)$$

Functions to simplify calculation:

$$K(X) = \cosh(MX) + B\sinh(MX) \quad (14)$$

$$G(X) = -(B\cosh(MX) + \sinh(MX)) \quad (15)$$

$$B = \frac{U_1 - \cosh(MX_1)}{\sinh(MX_1)} \quad (16)$$

The dimensionless groups were brought into governing equations and boundary conditions. First, the Poiseuilles Law was used to relate the pressure to the mean flow velocity with eqn. (4) to give:

$$\frac{d^2\langle U_x\rangle}{dX^2} = M^2\langle U_x\rangle \quad (17)$$

where $M^2 = \frac{16\kappa}{R}$

Then three functions, (14) - (16), were used to simplify the solutions proposed by Granger leading to the given below:

$$U_X(X,Y) = \quad (18)$$

$$2K(1-Y^2) + \frac{MKGRe}{72} \times (29 - 36Y^2 + 9Y^4 - 2Y^6) + \frac{KM^2}{8}(3 - 4Y^2 + Y^4) + \ldots$$

$$U_Y(X,Y) =$$

$$\frac{MG}{2}(2Y - Y^3) + \frac{M^2K^2Re}{288}(K^2 + G^2) \times (58Y - 36Y^3 + 6Y^5 - 2Y^7) + \ldots \quad (19)$$

$$F(X,Y) =$$

$$\frac{G}{M} + \frac{MG}{4}(1 - Y^2) + \frac{M^2K^2Re}{192} \times (12Y^2 - 9Y^4 + 2Y^6 - 5) + \ldots \quad (20)$$

The particle trajectory (targets to be separated) is the key criteria affecting the performance. The analytical solution is solved by combining (18) and (19).

$$Y = \sqrt{1 - \sqrt{\left\{\frac{Y_0^2(2 - Y_0^2)}{\cosh(MX) + B\sinh(MX)}\right\}}} \quad (21)$$

To sum up, Y means where particle is located in y direction from the center point in the ratio of column's radius. Y_0 means particle's Y position in the inlet of column. X means how far the particle travels in the ratio of column's length. All of them are in a dimensionless form. The model of particle's trajectory can be used to find out critical factors regarding device's performance in this work.

Three factors: column length, radius of the channel and flow rate were compared as shown in Fig. S15. In Figure S15a, the y-axis means the minimum inlet position of particles to interact with the porous wall and the x-axis means how far particles travel through the column. Taking x=0.25 as an example, only particles enter at position around 0.9 radius from the center point would interact with the porous wall when travel through 1/4th of the column. Namely, only 10% of particles would interact with the porous wall under this condition. Therefore, in the laminar flow condition, there may be 30-90% of particles leave the column without touching the porous wall. This model points out an important message about the limiting factor to be macroscopic design instead of adsorbent's capacity. In Figure S15 b and c, we further studied the relationship of the radius of the channel and flow rate with particles' Y position. Lines indicate particles entering the column from different inlet points. From these figures, the boundary layer is related to column length the most, then flow rate, and the last radius of the channel. The model points out the impact of boundary layer and provides guidance for future optimization. We show that macroscopic design as a new experimental degree of freedom for micro-/mesoporous separation devices actually plays a critical role.

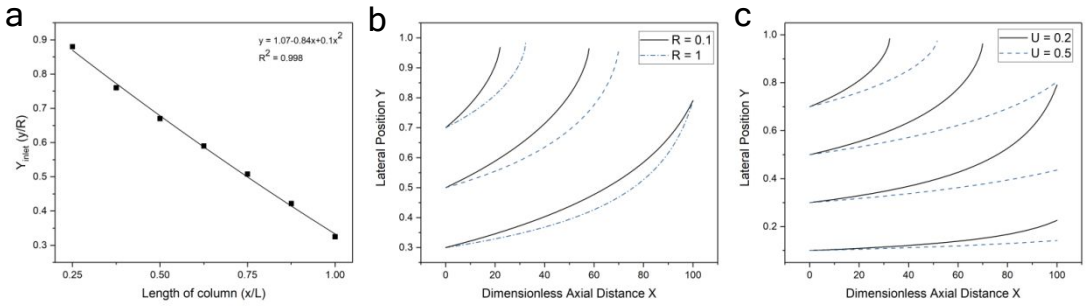

Figure S15. Plot of particle trajectories profiles with **a,** length of column, **b,** radius of the channel and **c,** flow rate. The y-axis numbers in **a** mean the minimum inlet position of a particle to touch the wall before leaving the column. Therefore, for column length = 0.25, only 10% of particles touch the wall. For column length = 1, 70% of particles touch the wall.

8. REFERENCES

1. Užarević, K. *et al.* Mechanochemical and Solvent-free Assembly of Zirconium-based Metal–organic Frameworks. *Chemical Communications* **52,** 2133–2136 (2016).
2. Huang, J.-Y. *et al.* Three-Dimensional Printing of Hierarchical Porous Architectures. *Chem. Mater.* **31,** 10017–10022 (2019).
3. Granger, J., Dodds, J. & Midoux, N. Laminar Flow in Channels with Porous Walls. *The Chemical Engineering Journal* **42,** 193–204 (1989).